


Nanoscale hyperspectral imaging of amyloid secondary structures in liquid

Journal Article

Author(s):

Lipiec, Ewelina; Kaderli, Janina; Kobierski, Jan; Riek, Roland; Skirlinska-Nosek, Katarzyna; Sofinska, Kamila; Szymonski, Marke; Zenobi, Renato 

Publication date:

2021-02-23

Permanent link:

<https://doi.org/10.3929/ethz-b-000441973>

Rights / license:

[In Copyright - Non-Commercial Use Permitted](#)

Originally published in:

Angewandte Chemie. International Edition 60(9), <https://doi.org/10.1002/anie.202010331>

Supporting Information
©Wiley-VCH 2019
69451 Weinheim, Germany

Nanoscale hyperspectral imaging of the amyloid secondary structure in liquid

Ewelina Lipiec, Janina Kaderli, Jan Kobierski, Roland Riek, Katarzyna Skirlińska-Nosek, Kamila Sofińska, Marek Szymoński, and Renato Zenobi*

Abstract: Abnormal aggregation of amyloid- β is a very complex and heterogeneous process. Due to methodological limitations, the aggregation pathway is still not fully understood. In this communication a new approach is presented in which the secondary structure of single amyloid- β aggregates is investigated with tip-enhanced Raman spectroscopy (TERS) in a liquid environment. This methodology provided more information about the secondary structure of proteins and peptides than TERS data acquired in dry conditions. Clearly resolved TERS signatures of the amide I and amide III bands enabled a detailed analysis of the molecular structure of single aggregates at each phase of the primary aggregation of amyloid- β . Notably, a β -sheet rearrangement from antiparallel in protofibrils to parallel in fibrils is directly observed. This study allows for better understanding of Alzheimer's disease etiology and the methodology can be applied in studies of other neurodegenerative disorders.

DOI: 10.1002/anie.2016XXXXX

Table of Contents

Experimental Procedures.....	2
Substrates preparation.....	2
Samples preparation.....	2
AFM imaging in liquid.....	2
TERS probes preparation.....	2
TER spectra acquisition.....	2
Data Processing.....	3
DFT calculation procedures.....	3
Results and Discussion.....	3
Topography analysis – Figure 1D and E detailed description.....	3
Bands assignment.....	3
Aggregation of A β ₁₋₄₂ - AFM studies.....	5
Classification of spectra of oligomers, fibrils and protofibrils.....	6
TER spectra acquired from individual A β ₁₋₄₂ aggregates in liquid.....	6
Theoretical Raman spectra.....	7
A comparison of TER spectra acquired in air and in liquid.....	8
Derivatives of TER spectra.....	9
References.....	10
Author Contributions.....	11

Experimental Procedures

Substrates preparation

The flame-annealed template stripped gold substrates were prepared according to the procedure reported by Banner *et al.*^[1] Briefly, Si wafers after careful cleaning in acetone, ethanol, and deionised water and drying were coated with a 100 nm gold layer using a deposition rate of 0.03 - 0.04 nm/s. The gold coated Si-wafers were flame-annealed using a Bunsen burner powered by natural gas for 4 mins. Then the flame-annealed gold surfaces were glued to clean Si-wafers, with a thin layer of UHU® glue and pressed tightly. The glue was allowed to dry overnight under ambient conditions and the gold substrate templates were stored under vacuum until use. Before the sample deposition, each gold-coated Si-wafer was stripped off using a razor blade, exposing a contamination-free and flat substrate.

Samples preparation

The A β ₁₋₄₂ solution was prepared according to the protocol, which was applied and described in details in our previous studies.^[2] A 5 mM solution of A β ₁₋₄₂ in DMSO (DMSO; \geq 99.8 % (GC), for UV-spectroscopy, Sigma Aldrich) was prepared and stored at -20 °C. Such prepared stock solution was diluted to a final concentration of 100 μ M using either freshly prepared 10 mM HCl in milli-Q water (pH 2.0) or phosphate buffer (pH 7.4) for comparison. The resulting A β ₁₋₄₂ solution was incubated at 37 °C in the darkness for 24 hours.

A template stripped gold substrate was glued to the middle of the liquid cell AFM sample holder. A droplet (30 - 40 μ L) of A β ₁₋₄₂ solution was deposited on the substrate for 40 - 60 mins at ambient temperature. Subsequently the substrate was rinsed with 0.5 mL milli-Q water to remove the excess of the peptide, which did not adsorb on the gold surface. Then the liquid cell was immediately filled with milli-Q water to avoid changes in peptide conformation upon drying.

Comprehensive studies of such prepared A β ₁₋₄₂ solutions were earlier performed. The individual steps of the aggregation were followed by the surface independent method ATR-FTIR and also AFM measurements under ambient conditions. Spectra and images were acquired from peptide aggregating for 0, 1, 2, 4, 6, 12, 18, 24, 36 h, and after 7 days. The detailed description of these measurements and their results are presented in our previous article.^[2] The ATR-FTIR spectra of A β ₁₋₄₂ prepared at pH 2 and pH 7.4 did not display any conformational differences suggesting alternative aggregation pathway.

AFM imaging in liquid

The AFM image in Figure 1 D was acquired in tapping mode in water environment with 512 x 512 pixels and a 0.5 Hz scanning rate using probes dedicated to measurements in liquids supplied by Veeco.

AFM maps presented in Figure 2 and 3 (main text) and FigureS2-S4, were acquired in tapping mode (with 512 x 512 pixels and a 0.2-0.5 Hz scanning rate) just before TER maps acquisition using VIT P C-A, NT-MDT coated with Ti/Au according to the procedure described below.

TERS probes preparation

AFM cantilevers (VIT P C-A, NT-MDT) were coated with 5 nm of a Ti adhesion layer and then with 20 - 25 nm of Au using a constant deposition rate of 0.03 - 0.04 nm/s, under 10⁻⁶ mbar vacuum.

TER spectra acquisition

The measurements were carried out on a Ntegra Spectra Upright instrument (NT-MDT, Zelenograd, Russia) integrated with a solar TII Raman spectrometer and an Andor Newton 971 UVB CCD camera (cooled to -86 °C). The system was equipped with a specially

SUPPORTING INFORMATION

designed head for AFM in liquids. A red HeNe laser (632.8 nm) was applied (139 - 1209 μ W). Single TER spectra, arrays of spectra and maps were collected in the spectral range of 150 - 1800 cm^{-1} with a spectral resolution of 2cm^{-1} . The acquisition time of a single spectrum was set to 5 - 15 s depending on the signal-to-noise ratio (SNR).

Data Processing

All the topographic AFM images were flattened by a 2nd or 3rd order polynomial correction using SPIP software. TER spectra and maps were processed using Matlab (version 8.3.0, R2019a) in combination with the PLS toolbox and Mia toolbox (<http://www.eigenvector.com/>). In order to obtain a high enhancement factor, a metallic (gold) substrate was used (gap-mode TERS). In this configuration, the locally induced gap plasmon has a critical impact on the TERS enhancement. The baseline and SNR vary in the spectra acquired from various places on the sample. Therefore, in order to avoid an influence of the baseline and the noise on the results of Hierarchical Cluster Analysis, and also to present multiple spectra in one plot for comparison (e.g. Figure 2, Figure S3) and for demonstrating spectral changes related to the secondary structure, minimal processing of the spectra, which did not introduce artifacts and did not affect peak ratios, was applied. First cosmic rays were removed and the Savitzky–Golay algorithm was applied for smoothing (2nd order polynomial, 9-15 smoothing points). Then a baseline correction (2nd - 4th order polynomial) and vector normalization (1750 – 650 cm^{-1}) were performed.

DFT calculation procedures

Geometry optimization and frequency calculations of L-alanyl-L-phenylalanine (Ala-Phe) peptide were performed using Density Functional Theory (DFT) modeling through the Gaussian 16 software package.^[3] All calculations were performed using the B3LYP functional^[4-7] with 6-311+G(d,p) basis set. Systems were optimized using the default UltraFine integration grid, default integral cutoffs and a combination of EDIIS and CDIIS tight convergence procedures, with no damping or Fermi broadening.

Three systems were optimized: Ala-Phe in a vacuum, Ala-Phe in the presence of two explicit water molecules, and Ala-Phe in the presence of water as solvent, using the Polarizable Continuum Model (see). For the model with explicit water molecules, the base superposition error (BSSE) was eliminated by using the counterpoise correction. The raw frequencies obtained from the vibrational simulation were scaled by the factor 0.989, found on the basis of a 1004 cm^{-1} peak corresponding to CC breathing in the aromatic ring.^[8]

The theoretical Raman intensities were calculated according to the formula ^[9]:

$$I_i^R = C(v_0 - v_i)^4 v_i^{-1} B_i^{-1} S_i$$

where C is a constant given in arbitrary units, S_i and v_i are the calculated Raman scattering activity and the frequency of the normal mode Q_i , respectively. v_0 is the frequency of the laser excitation line. In this work, the 15 798 cm^{-1} frequency was incorporated to calculations, what corresponds to 633 nm, a wavelength emitted by diode laser used in experiments. B_i is a temperature factor which accounts for the intensity contribution of excited vibrational states and is represented by the Boltzmann distribution:

$$B_i = 1 - \exp\left(-\frac{hcv_i}{kT}\right)$$

where h, k, c are Planck's constant, the Boltzmann constant, and the speed of light, respectively. T stands for temperature, which was 293 K.

Results and Discussion**Figure 1D and E detailed description**

Profiles 1-3 are clearly smoother and thinner in comparison to profiles 4-6 and 7-9, while their height is between that of profiles 7-9 (the lowest species) and 4-6 (the highest objects). The morphology of profiles 1-3 indicates the most ordered structure characteristic of mature fibrils with a cross- β arrangement along the fibril axis. The biggest height and diameter of profiles 4-6 can be associated with a less ordered structure of protofibrils consisting of segments carrying a parallel or antiparallel distribution of β -sheets, depending on the aggregation pathway. The lowest profiles (7-9) are related to intermediates occurring at the initial stage of the amyloid aggregation process, oligomers, usually built of few monomer units.

Band assignments

Table S1. The band assignments for various amyloids obtained by Raman nanospectroscopies including AFM-TERS in air and liquid and STM-TERS compared with conventional Raman measurements.

Band assignment	AFM-TERS in air ^[2,10]	AFM-TERS in liquid	STM-TERS in air	Raman
	Band frequency [cm^{-1}]			
amide I (1700 - 1600 cm^{-1}): vibrations: 80% $\nu(\text{C}=\text{O})$, 10% $\nu(\text{C}-\text{N})$, 10% $\delta(\text{N}-\text{H})$				
extended β -strand, β -sheet or turn	-	1695-1692	-	1685-1674- (α -syn ^[11])

SUPPORTING INFORMATION

anti-parallel β -sheet, fibril core β -sheet	1680–1660 ($A\beta^{[2,10]}$, hIAPP ^[12])	1684/1625	-	1667 (α -syn ^[11]) 1675-1673 ^[13]
β -turns/unordered coils or β -hairpin	1655–1630 ($A\beta^{[2,10]}$)	1662-1639	-	1665-1654 ^[14] 1670-1660 ^[13]
parallel β -sheet		1627	-	
Tyr and Phe amino acid residues (high in native form)	-	1616-1612	-	1616 ^[14] 1616 (α -syn ^[11])
amide II (1580 - 1500 cm⁻¹), vibrations: 60% δ(N-H), 40% ν(C-N)				
	1560-1590 (insulin ^[15])	1586-1580	-	
unstructured coils, fibril core β -sheet	1534-1552 (insulin ^[15])	1568-1564	-	~1550 ^[14] 1561-1548 ^[13] , 1560-1553 ^[13]
anti-parallel β -sheet	1523-1528 (insulin ^[15])	1533-1532	-	
histidine				
His (NH)	1515-1490 (insulin ^[15]) 1494 (hIAPP ^[12])	1506-1503		
C-H vibrational modes				
CH ₃ , CH ₂ scissoring motions	1428 ($A\beta^{[2,10]}$)	1485-1432	-	1450 ^[14]
Cα-H/N-H				
β -sheets bending	1364 ($A\beta^{[2,10]}$) 1390 (HEWL ^[16])	1394-1391	-	1390 ^[14]
amide III (1340 - 1200 cm⁻¹), vibrations: 30% ν(C-N), 30% δ(N-H), 10% ν(CH₃-C), 10% δ(O=C-N), 20% other				
C=N and C-N stretching (histidine)	1334 (± 3) ($A\beta^{[2,10]}$) 1331 (hIAPP ^[12])	1345		
CH ₂ , Gly	1327-1310 (insulin ^[15])	1307-1303		
CH ₂	1290-1284 (insulin ^[15])	1289-1287		
turns/unstructured coils	1261–1248 ($A\beta^{[2,10]}$)	1269-1267		1260-1240 ^[13]
β -sheet	1250 ($A\beta^{[2,10]}$)			1253 ^[14] 1240 (α -syn ^[11])
anti-parallel β -sheet	1242–1233 ($A\beta^{[2,10]}$)	1235-1232		1233 ($A\beta^{[17]}$) 1241 (YEHKpp ^[18])
parallel β -sheet	1228–1218 ($A\beta^{[2,10]}$)	1224-1220		1214 ($A\beta^{[17]}$)
amino acids residues				
Tyr (side chain)	1204-1196 (insulin ^[15]) 1191-1186 (insulin ^[15])	1203 1175-1173		
Arg (=NH ₂ ⁺)	1170-1166 (insulin ^[15])	1163-1158		
Lys (NH ₃ ⁺)	1153-1145 (insulin ^[15])	1144-1141		
Arg (=NH ₂ ⁺)	1094-1088 (insulin ^[15])	1099-1097		
Asn, Gln (NH ₃ ⁺)	1140-1121 (insulin ^[15]) 1078-1060 (insulin ^[15])	1118-1116 1076-1065		
Phe (ring)	1038 (hIAPP ^[12])	1056-1051 1038-1035 ^[19]		
phenylalanine				
phenylalanine ring breathing mode	1007-1004 ($A\beta^{[2,10]}$) 1010 (hIAPP ^[12])	1003-1001	1004 ($A\beta^{[2,20]}$)	1616 ^[14]
amino acids residues				
valine		934-931 ^[21]		
Tyr (ring breathing)	868-865, 848-845/ 826-819 (insulin ^[15]) 856 / 826 (hIAPP ^[12])	877-840/ 823-817		
C-S stretching vibration of methionine (or cysteine)	775-760 (insulin ^[15]) 767 (± 3) ($A\beta^{[2,10]}$) 667-657 (insulin ^[15])	767-766 661-658		

v – stretching, δ – bending

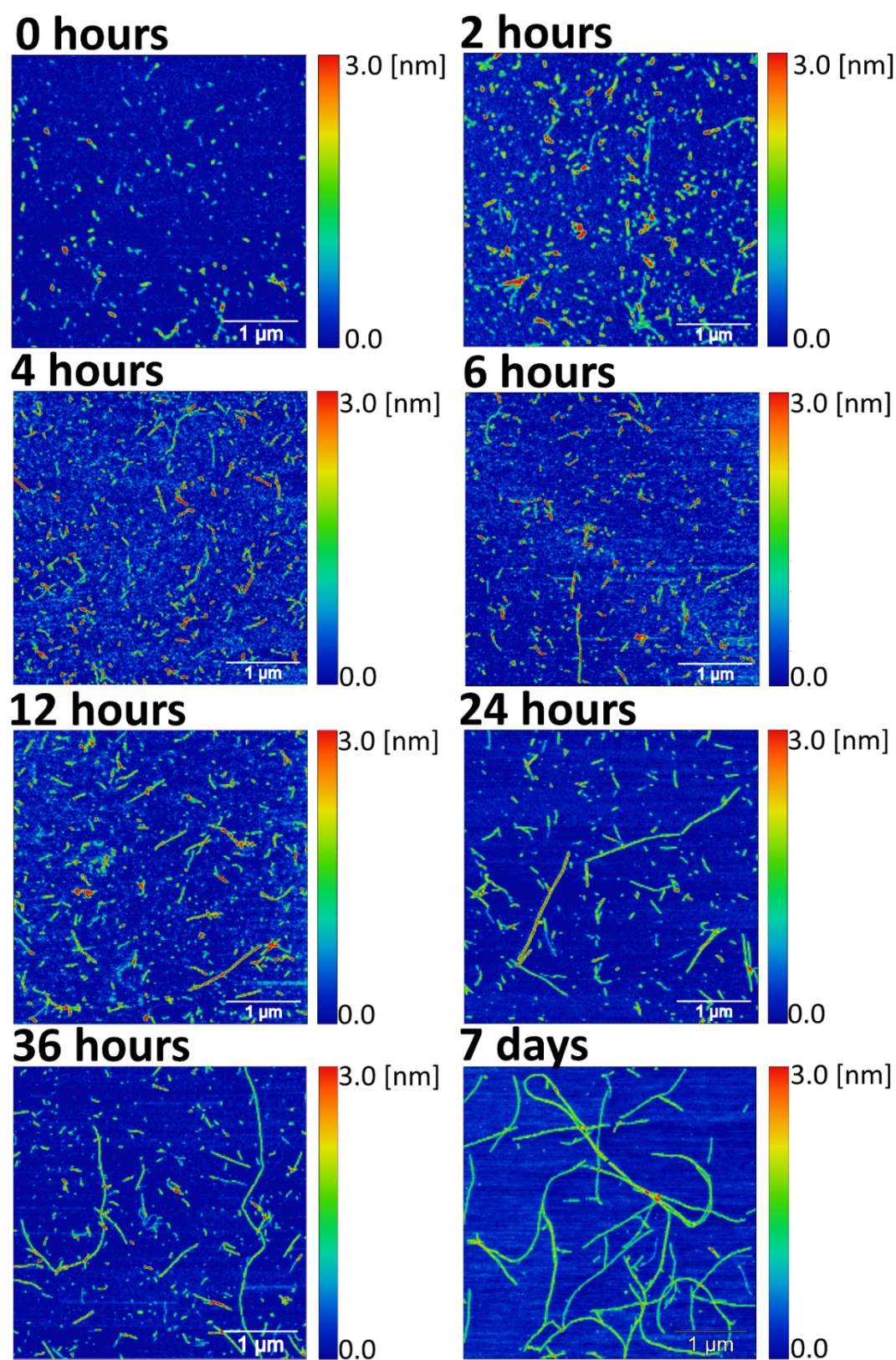
Aggregation of A β_{1-42} - AFM studies

Figure S1. Monitoring of morphological changes during the aggregation of A β_{1-42} .

SUPPORTING INFORMATION

According to the results reported in the literature, A β fibrillates,^[22] however, it also may form non-fibrous structures.^[23] We did not observe such unstructured aggregates possibly due to the applied of aggregation conditions. AFM imaging demonstrates the morphology of aggregating amyloids (Figure S1). After 7 days of incubation only fibrils were observed.

Classification of spectra of oligomers, fibrils and protofibrils

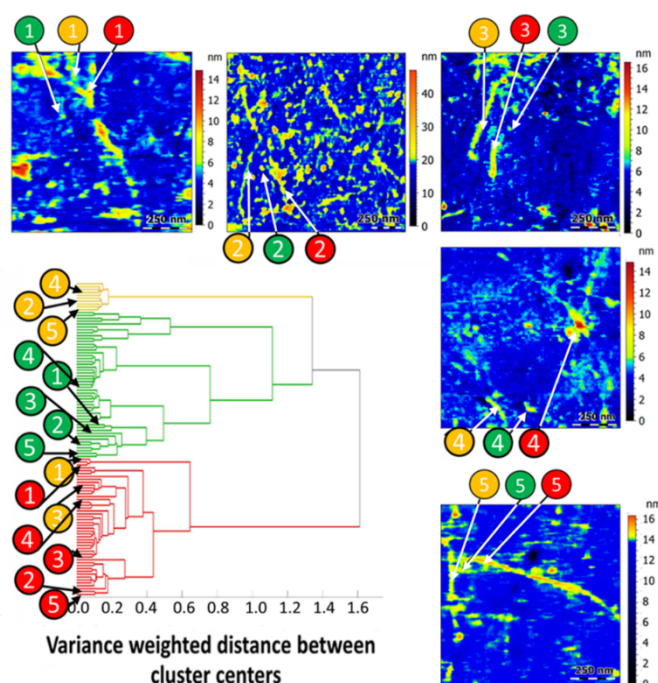


Figure S2. The results of a HCA analysis for randomly chosen TER spectra from Figure 1 with additional spectra acquired from fibrils (yellow), protofibrils (red) and oligomers (green), showing 87% correct classification. The locations of the spectra acquisition are presented in AFM topographies.

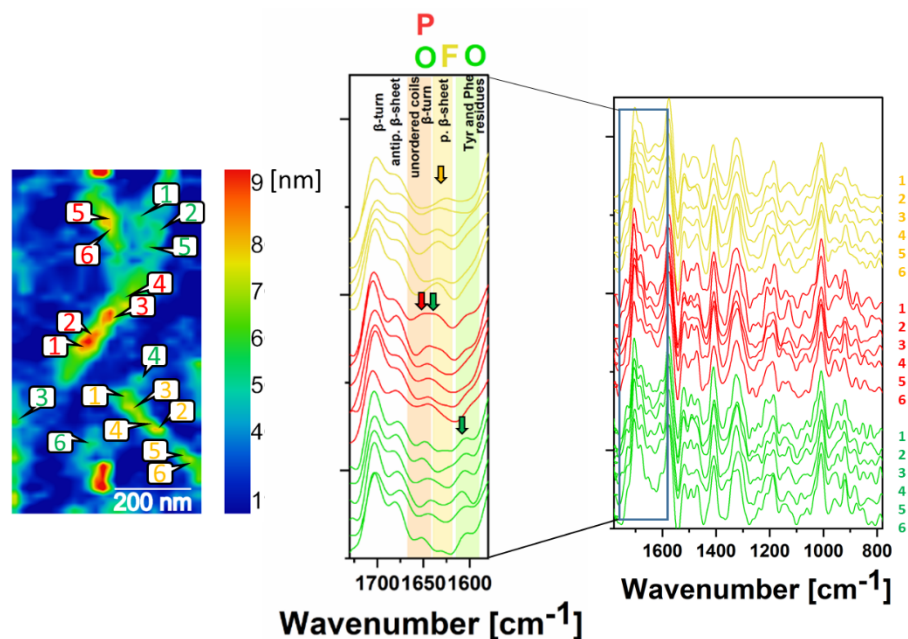
TER spectra acquired from individual A β ₁₋₄₂ aggregates in liquid

Figure S3. Individual TER spectra acquired from fibrils (yellow), protofibrils (red) and oligomers (green) with the locations of the spectra acquisition. The incubation time was 36 hours.

SUPPORTING INFORMATION

Theoretical Raman spectra

Raman spectra calculated for systems containing Ala-Phe peptide are shown in

Figure S4. Optimized structures of A) Ala-Phe in vacuum, B) Ala-Phe in vacuum with explicit water molecules (the dashed lines represent the hydrogen bonds), and C) Ala-Phe in water solvent.

Figure . A description of the bands is presented in **Error! Reference source not found.** Stretching vibrations of C=O bonds, in vacuum at 1817 cm^{-1} and 1743 cm^{-1} for phenylalanine and alanine, respectively, in the presence of water molecules are shifted to 1791 cm^{-1} and 1729 cm^{-1} . Optimization of the system (see Figure S4) resulted in the placement of water molecules near the carbonyl groups of the polypeptide, and thus hydrogen bonds. This, in turn, implies a wavenumber decrease.^[24–26] The shift is even more apparent when the model of the water solvent is applied. Additionally, as a consequence of hydrogen bonding,^[26] the increase of the frequency of scissoring vibration NH_2 in alanine was observed, from 1653 cm^{-1} to 1673 cm^{-1} , when water molecules were added to the model. Neither the addition of water molecules nor the utilization of solvent model caused significant shifts in the frequency of stretching and scissor vibrations in the phenylalanine aromatic ring.

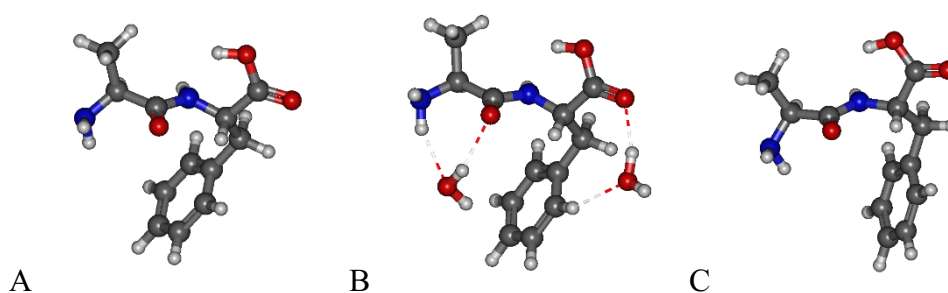
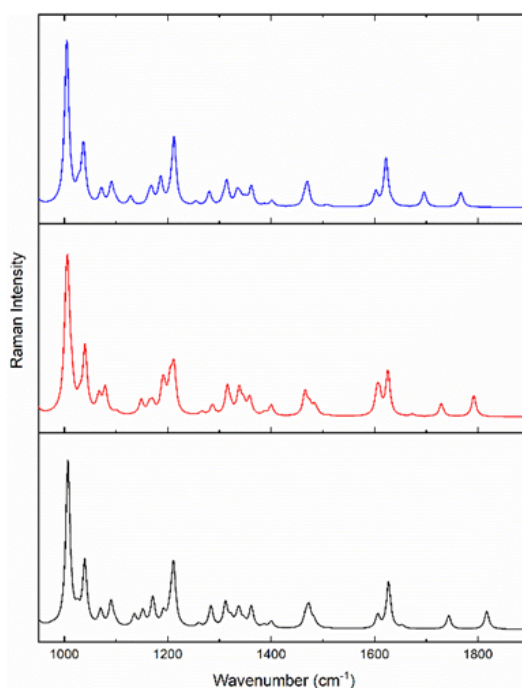


Figure S4. Optimized structures of A) Ala-Phe in vacuum, B) Ala-Phe in vacuum with explicit water molecules (the dashed lines represent the hydrogen bonds), and C) Ala-Phe in water solvent.



SUPPORTING INFORMATION

Figure S5. Calculated Raman spectra of Ala-Phe in vacuum (bottom-black), Ala-Phe in vacuum with explicit water molecules (middle-red), and Ala-Phe in water solvent (top-blue).

Table S2. Band assignments for calculated Raman spectra of Ala-Phe in vacuum, Ala-Phe in vacuum with explicit water molecules, and Ala-Phe in water solvent.

Ala-Phe in vacuum	Ala-Phe with water molecules	Ala-Phe in water	Assignment	Amino acid
Wavenumber (cm ⁻¹)				
1817	1791	1767	v(C=O), δ(COH)	Phenylalanine
1743	1729	1695	δ(CNH)	Phenylalanine
1653	1673	1633	v(C=O)	Alanine
1627	1625	1622	δ(NH ₂)	Alanine
1606	1604	1602	v(CC)	
1210	1211	1211	δ(CC)	Phenylalanine (ring)
1039	1039	1036	v(CC)	
1006	1006	1004	CC breathing	

A comparison of TER spectra acquired in air and in liquid

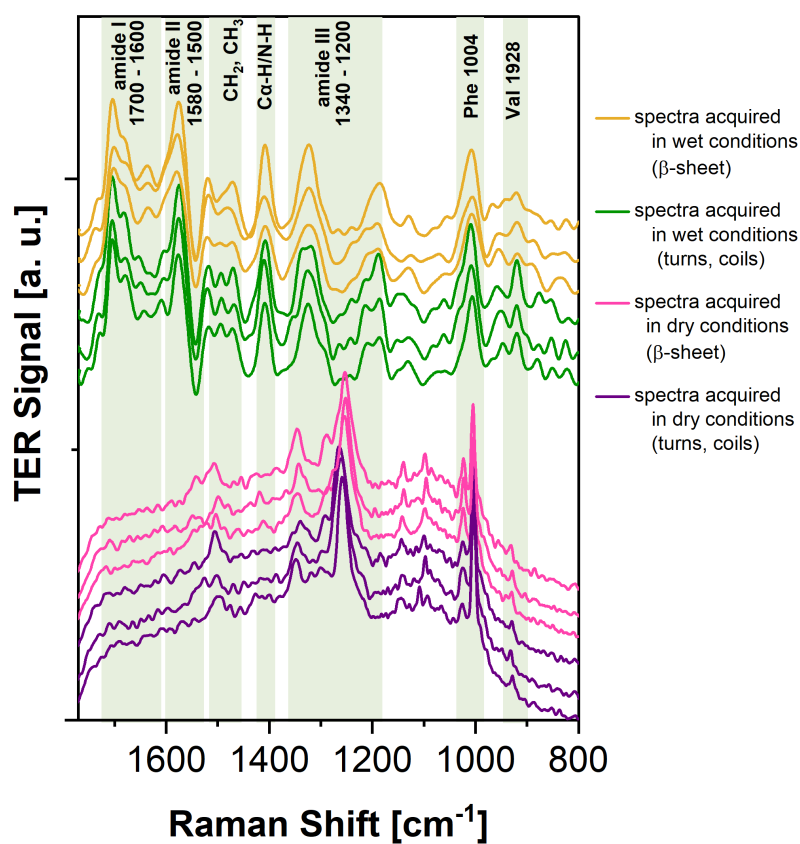


Figure S6. A direct comparison of spectra of Aβ₁₋₄₂ aggregating for 36 hours and then deposited onto the gold substrate, acquired in ambient conditions and in liquid.

SUPPORTING INFORMATION

Figure S6 presents TER spectra acquired from samples prepared in an analogous fashion in air (pink and violet) and in liquid (yellow and green). The absence of the amide I band is clearly visible in the spectra acquired in ambient conditions, in contrast to the data collected in liquid. Both groups of spectra indicate the presence of β -sheet and turns/coils conformations, however, TERS markers of spectra acquired in air and in liquid are different. In air, the position of the amide III above 1255 cm^{-1} is characteristic for turns/random coil and below 1255 cm^{-1} for β -sheet conformation.^[27] In spectra acquired in liquid, the presence of a peak at 1626 cm^{-1} is attributed to parallel β -sheet conformation. The effect of protein backbone hydration on the amide III band is visible. Observed shifts and intensity changes are caused by hydrogen bonding with both the C=O and N–H functional groups. Precisely, the formation of a $\text{C}=\text{O}\cdots\text{H}_2\text{O}$

bond causes a decrease of the C–N bond length, in contrast to the formation of a hydrogen bond between N–H and H_2O , which increases the length of the N–H bond.

The presence of the amide I band in the spectra acquired in liquid indicates that the peptide backbone is not subjected to photoinduced damage. There are several physical phenomena that are responsible for the protective role of the solvent:

- (i) The high heat capacity of liquid causes efficient heat dissipation from the tip, resulting in a decrease of the effective temperature of the plasmonic nanostructure.^[28] A decrease of thermal diffusion of surface atoms stabilizes the crystal facets of the plasmonic nanostructure, improving the stability of the TERS signal.^[29,30]
- (ii) The rate of plasmon-induced sample damage of the peptide chemical structure can be indirectly reduced or slowed down by the temperature decrease due to effective heat transfer in liquids. Photoinduced damage is driven by transfer of plasmon-induced hot carriers from the plasmonic nanostructure to the analyzed molecules,^[31,32] including peptides.^[33] This reaction rate depends strongly on the temperature due to a synergy between electronic and vibrational excitations.^[34,35]
- (iii) The increasing temperature leads to the formation of carbonaceous species under the tip.^[31,36] Even slight traces of carbonaceous contaminations are observable as rapidly fluctuating peaks, which, averaged over many spectra, result in a broad D-band (1360 cm^{-1}) and G-band (1580 cm^{-1}).^[36] A temperature decrease in the hot spot due to high heat capacity of the liquid prevents undesired sample desorption.^[28]
- (iv) The oxygen and hydroxyl radicals may also contribute to the degradation of the analytes. The exposure of the peptide backbone to such radicals in liquids is lower than in air due to their different availability.^[37]

Derivatives of TER spectra

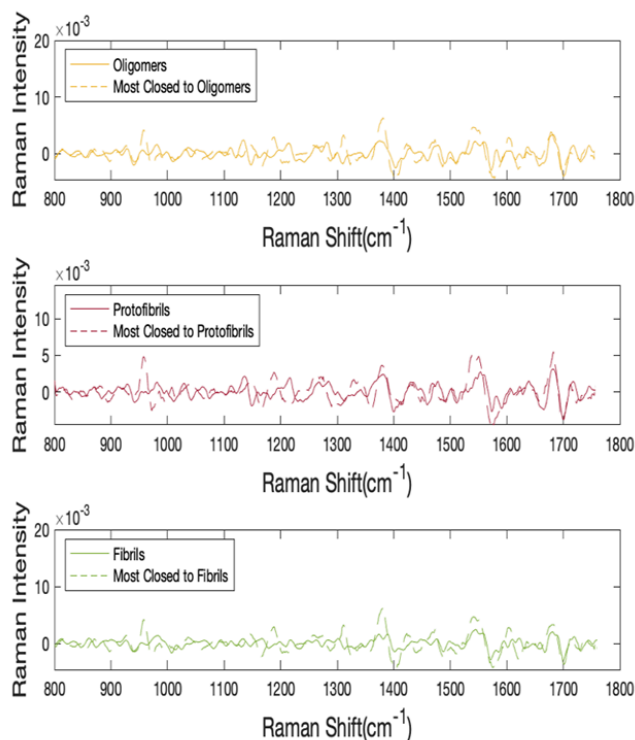


Figure S7. Second derivatives of marker TER spectra of oligomers, protofibrils and fibrils in comparison with highly correlated spectra extracted from TER map (Fig. 3 upper panel).

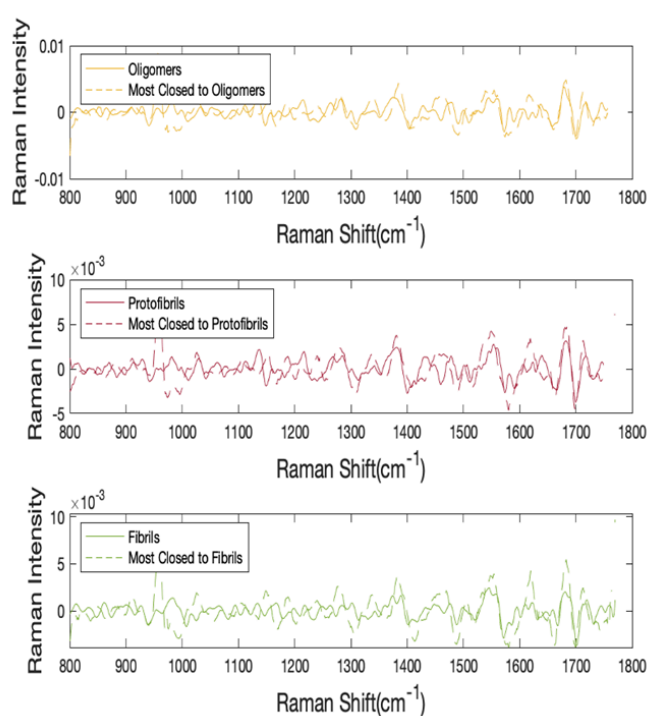


Figure S8. Second derivatives of marker TER spectra of oligomers, protofibrils and fibrils in comparison with highly correlated spectra extracted from TER map (Fig. 3 lower panel).

References

- [1] L. T. Banner, A. Richter, E. Pinkhassik, *Surf. Interface Anal.* **2009**, *41*, 49–55.
- [2] E. Lipiec, D. Perez-Guaita, J. Kaderli, B. R. Wood, R. Zenobi, *Angew. Chemie* **2018**, *130*, 8655–8660.
- [3] D. J. Frisch, M. J.; Trucks, G. W.; Schlegel, H. B.; Scuseria, G. E.; Robb, M. A.; Cheeseman, J. R.; Scalmani, G.; Barone, V.; Petersson, G. A.; Nakatsuji, H.; Li, X.; Caricato, M.; Marenich, A. V.; Bloino, J.; Janesko, B. G.; Gomperts, R.; Mennucci, B.; Hratch, *Gaussian 16, Revision B.01*, Gaussian, Inc., Wallingford CT, **2016**.
- [4] A. D. Becke, *J. Chem. Phys.* **1993**, *98*, 5648–5652.
- [5] C. Lee, W. Yang, R. G. Parr, *Phys. Rev. B* **1988**, *37*, 785–789.
- [6] S. H. Vosko, L. Wilk, M. Nusair, *Can. J. Phys.* **1980**, *58*, 1200–1211.
- [7] P. J. Stephens, F. J. Devlin, C. F. Chabalowski, M. J. Frisch, *J. Phys. Chem.* **1994**, *98*, 11623–11627.

SUPPORTING INFORMATION

- [8] M. Baranska, *Optical Spectroscopy and Computational Methods in Biology and Medicine*, Springer Netherlands, Dordrecht, **2014**.
- [9] D. Michalska, R. Wysokiński, *Chem. Phys. Lett.* **2005**, *403*, 211–217.
- [10] S. Bonhommeau, D. Talaga, J. Hunel, C. Cullin, S. Lecomte, *Angew. Chemie - Int. Ed.* **2017**, *56*, 1771–1774.
- [11] N. C. Maiti, M. M. Apetri, M. G. Zagorski, P. R. Carey, V. E. Anderson, *J. Am. Chem. Soc.* **2004**, *126*, 2399–2408.
- [12] C. C. vandenAkker, T. Deckert-Gaudig, M. Schleegeer, K. P. Velikov, V. Deckert, M. Bonn, G. H. Koenderink, *Small* **2015**, *11*, 4131–4139.
- [13] V. A. Shashilov, V. Sikirzhitski, L. A. Popova, I. K. Lednev, *Methods* **2010**, *52*, 23–37.
- [14] D. Kourouski, R. P. Van Duyne, I. K. Lednev, *Analyst* **2015**, *140*, 4967–4980.
- [15] T. Deckert-Gaudig, D. Kourouski, M. A. B. Hedegaard, P. Singh, I. K. Lednev, V. Deckert, *Sci. Rep.* **2016**, *6*, 1–9.
- [16] M. F. Rosario-Alomar, T. Quiñones-Ruiz, D. Kourouski, V. Sereda, E. B. Ferreira, L. De Jesús-Kim, S. Hernández-Rivera, D. V. Zagorevski, J. López-Garriga, I. K. Lednev, *J. Phys. Chem. B* **2015**, *119*, 1265–1274.
- [17] L. A. Popova, R. Kodali, R. Wetzel, I. K. Lednev, *J. Am. Chem. Soc.* **2010**, *132*, 6324–6328.
- [18] V. Sikirzhitski, N. I. Topilina, S. Higashiya, J. T. Welch, I. K. Lednev, *J. Am. Chem. Soc.* **2008**, *130*, 5852–5853.
- [19] B. Sjöberg, S. Foley, B. Cardey, M. Enescu, *Spectrochim. Acta - Part A Mol. Biomol. Spectrosc.* **2014**, *128*, 300–311.
- [20] M. Paulite, C. Blum, T. Schmid, L. Opilik, K. Eyer, G. C. Walker, R. Zenobi, *ACS Nano* **2013**, *7*, 911–920.
- [21] A. Rygula, K. Majzner, K. M. Marzec, A. Kaczor, M. Pilarczyk, M. Baranska, *Raman Spectroscopy of Proteins: A Review*, John Wiley & Sons, Ltd, **2013**.
- [22] L. Gremer, D. Schölzel, C. Schenk, E. Reinartz, J. Labahn, R. B. G. Ravelli, M. Tusche, C. Lopez-Iglesias, W. Hoyer, H. Heise, et al., *Science (80-)*. **2017**, *358*, 116–119.
- [23] D. Jiang, I. Rauda, S. Han, S. Chen, F. Zhou, *Langmuir* **2012**, *28*, 12711–12721.
- [24] I. S. Ryu, X. Liu, Y. Jin, J. Sun, Y. J. Lee, *RSC Adv.* **2018**, *8*, 23481–23488.
- [25] R. Ramaekers, J. Pajak, B. Lambie, G. Maes, *J. Chem. Phys.* **2004**, *120*, 4182–4193.
- [26] D. Lin-Vien, N. B. Colthup, W. G. Fateley, J. G. Grasselli, in *Handb. Infrared Raman Charact. Freq. Org. Mol.*, Elsevier, **1991**, pp. 155–178.
- [27] E. Lipiec, D. Perez-Guaita, J. Kaderli, B. R. Wood, R. Zenobi, *Angew. Chemie* **2018**, *130*, 8655–8660.
- [28] Z. C. Zeng, H. Wang, P. Johns, G. V. Hartland, Z. D. Schultz, *J. Phys. Chem. C* **2017**, *121*, 11623–11631.
- [29] N. C. Lindquist, C. D. L. de Albuquerque, R. G. Sobral-Filho, I. Paci, A. G. Brolo, *Nat. Nanotechnol.* **2019**, *14*, 981–987.
- [30] F. Benz, M. K. Schmidt, A. Dreismann, R. Chikkaraddy, Y. Zhang, A. Demetriadou, C. Carnegie, H. Ohadi, B. De Nijs, R. Esteban, et al., *Science (80-)*. **2016**, *354*, 726–729.
- [31] J. Szczerbiński, L. Gyr, J. Kaeslin, R. Zenobi, *Nano Lett.* **2018**, *18*, 6740–6749.
- [32] R. Wang, J. Li, J. Rigor, N. Large, P. Z. El-Khoury, A. Y. Rogachev, D. Kourouski, *J. Phys. Chem. C* **2020**, *124*, 2238–2244.
- [33] J. Szczerbiński, J. B. Metternich, G. Goubert, R. Zenobi, *Small* **2020**, *16*, 1905197.
- [34] L. Zhou, D. F. Swearer, C. Zhang, H. Robotjazi, H. Zhao, L. Henderson, L. Dong, P. Christopher, E. A. Carter, P. Nordlander, et al., *Science (80-)*. **2018**, *362*, 69–72.
- [35] X. Zhang, X. Li, M. E. Reish, D. Zhang, N. Q. Su, Y. Gutiérrez, F. Moreno, W. Yang, H. O. Everitt, J. Liu, *Nano Lett.* **2018**, *18*, 1714–1723.
- [36] K. F. Domke, D. Zhang, B. Pettinger, *J. Phys. Chem. C* **2007**, *111*, 8611–8616.
- [37] S. C. Huang, X. Wang, Q. Q. Zhao, J. F. Zhu, C. W. Li, Y. H. He, S. Hu, M. M. Sartin, S. Yan, B. Ren, *Nat. Commun.* **2020**, *11*, 1–8.

Author Contributions

E.L. and R.Z conceived and designed the experiments; E.L. and J. K. performed the experiments; E.L. and K.S-N analysed the data; E.L. and K.S. wrote the manuscript. J. K. performed and described the DFT calculations. All authors contributed to correcting the paper and to scientific discussions related to the data analysis and interpretation.